Volume 1
Number 2
1 March 2024
Pages 209–330

RSC Applied Interfaces

rsc.li/RSCApplInter

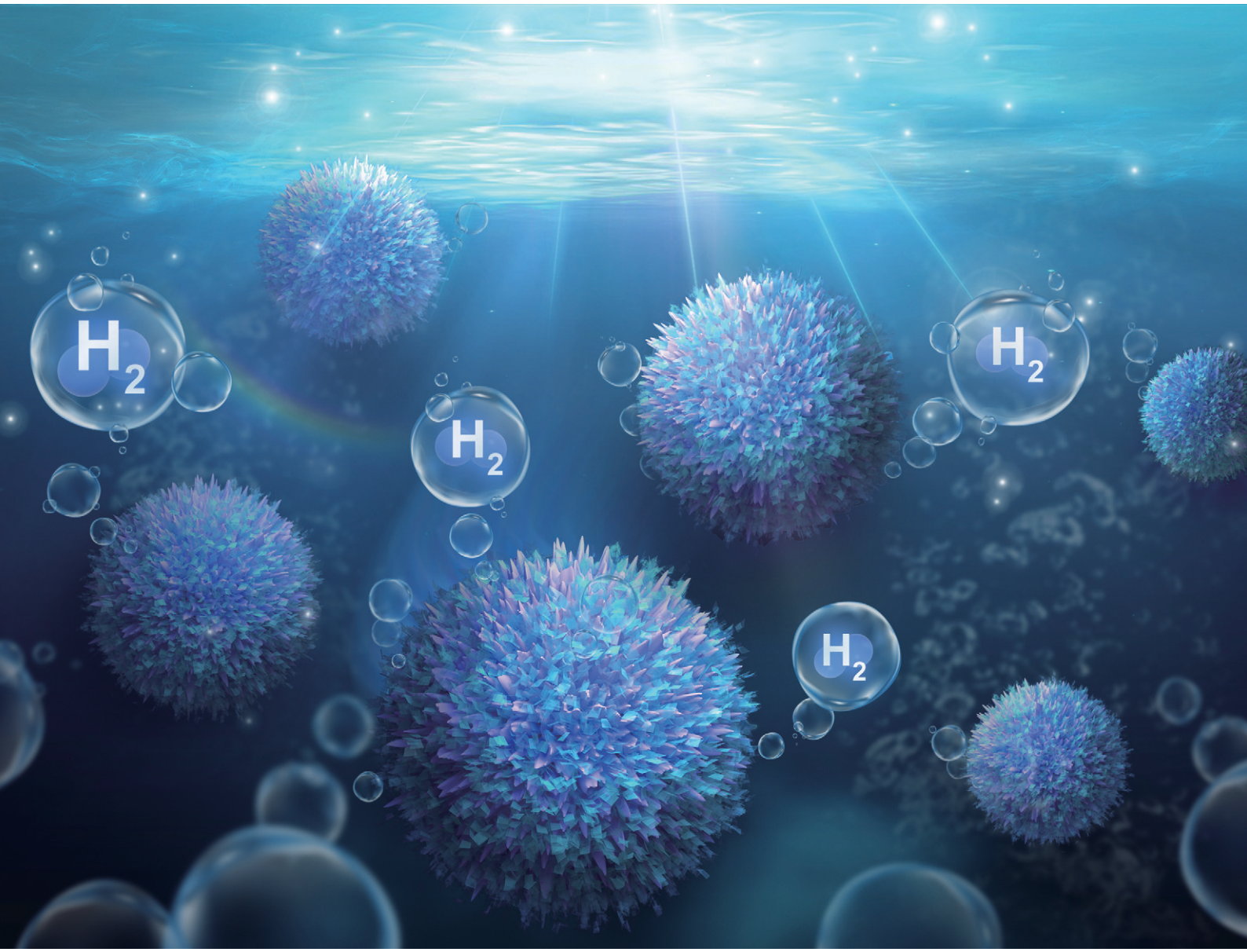

ISSN 2755-3701

ROYAL SOCIETY OF CHEMISTRY

PAPER

Liyong Ding, Juncheng Hu *et al.*
Construction of a hierarchical CoP@$ZnIn_2S_4$ heterojunction for photocatalytic hydrogen evolution

RSC Applied Interfaces

ROYAL SOCIETY OF CHEMISTRY

PAPER

View Article Online
View Journal | View Issue

Cite this: *RSC Appl. Interfaces*, 2024, **1**, 222

Construction of a hierarchical CoP@$ZnIn_2S_4$ heterojunction for photocatalytic hydrogen evolution†

Yuqin Liu,[a] Liyong Ding,*[b] Qian Xu,[c] Yu Ma[a] and Juncheng Hu *[a]

To relieve the present energy scarcity and environmental challenges, hydrogen formation *via* water decomposition utilizing sunlight is desirable. However, due to poor charge separation and low hydrogen production efficiency, conventional semiconductor photocatalysts are limited in practical applications. Herein, by introducing a spatial decoupling strategy, a core–shell CoP@$ZnIn_2S_4$ heterojunction photocatalyst is built through *in situ* formation of two-dimensional $ZnIn_2S_4$ (ZIS) nanosheets on a spiky CoP surface, achieving effective separation of the redox sites, resulting in a substantial enhancement of photocatalytic hydrogen formation efficiency. Notably, the optimized 5-CoP@ZIS photocatalyst exhibits a hydrogen production rate of 14.98 mmol g^{-1} h^{-1} with full solar spectrum illumination, which is 6.3-fold higher than the individual ZIS. These results exhibit that the increased efficiency is explained by the creation of the CoP@ZIS core–shell heterostructure, which strongly prevents the self-assembly and aggregation of the ZIS nanosheets, and offers enhanced light absorption and an abundance of reaction sites. The close interfacial contact facilitates the light-induced electron separation and transfer from ZIS to CoP, which synergistically yields an efficient hydrogen production performance. This work offers a highly effective method for the fabrication of powerful photocatalysts to realize light energy conversion.

Received 5th September 2023,
Accepted 5th October 2023

DOI: 10.1039/d3lf00157a

rsc.li/RSCApplInter

1. Introduction

As fossil energy usage rises and environmental issues become progressively more prominent, the pursuit for clean and sustainable alternative energy sources becomes increasingly pressing. Researchers have extensively recognized and predicted hydrogen as a renewable and clean new energy source.[1–6] Recently, researchers have developed a variety of hydrogen production technologies, including electrolysis of water, hydrogen synthesis from fossil raw materials, biomass hydrogen generation, and photocatalytic decomposition of water. Among them, solar-driven semiconductor-based fabrication of hydrogen through water decomposition is one of the greatest viable hydrogen production strategies due to the universality and inexhaustibility of sunlight. To date, numerous semiconductors with various bandgap energies, including oxides (ZnO, TiO_2 and Fe_2O_3),[7–9] sulfides (CdS, ZnS and MoS_2),[10–12] and carbon-based materials (graphene, g-C_3N_4),[13,14] *etc.*, have been produced and thoroughly investigated for photocatalytic water decomposition to produce hydrogen. However, on account of their restricted ability to absorb light and slow carrier dynamics, conventional single-component semiconductor photocatalysts typically exhibit inferior photocatalytic activity.[15] For example, ZnO, as a significant n-type semiconductor, has made many advances in photocatalytic hydrogen production due to its non-toxicity, easy-to-control morphology, and high redox potential. However, on account of its wide bandgap (~3.37 eV), the corresponding PHE process can only be carried out in the UV irradiation region, and most of the sunlight cannot be utilized, which severely limit the improvement of its photocatalytic hydrogen production efficiency.[16] As a result, it is critical to design and build efficient and robust photocatalysts.

Metal sulfides, particularly $ZnIn_2S_4$ (ZIS), are recognized to be potential photocatalysts with their minimal toxicity, appropriate bandgap width, and distinctive electro-optical characteristics, which have lately sparked renewed interest in photocatalytic generation of hydrogen.[17–19] However, due to the rapid complexation speed of photogenerated carriers and the scarcity of active surfaces, it has a low light utilization.[20] Furthermore, due to the accumulation of photogenerated cavities in ZIS-based catalysts, S^{2-} ions may combine with the

[a] *School of Chemistry and Materials Science, South-Central Minzu University, Wuhan 430074, China. E-mail: jchu@mail.scuec.edu.cn*
[b] *College of Chemical and Material Engineering, Quzhou University, Quzhou 324000, China. E-mail: liyongding1988@163.com*
[c] *Zhongnan University of Economics and Law, Wuhan 430073, China*

† Electronic supplementary information (ESI) available: Supplementary data includes experimental details (including characterization and photocatalytic H_2 evolution tests), SEM, XRD, TEM, HAADF-STEM, elemental mapping images and XPS spectra. See DOI: **https://doi.org/10.1039/d3lf00157a**

cavities and generate S, leading to serious photocorrosion processes, thereby shortening the durability of the photocatalysts and limiting their practical applications.[21] Impressively, the unique ultrathin 2D ZIS nanosheets not only have an extensive specific surface area for exposing numerous active regions, but also a significantly reduced photogenerated carrier migration distance.[22] However, individual 2D ZIS nanosheets are subject to self-assembly and aggregation, causing the development of 3D ZIS nanoflowers, which greatly restrict the ability of photogenerated carriers to separate, as well as minimize their photocatalytic capacity.[23] Therefore, it is critical to develop a strategy that can successfully prevent the aggregation of 2D ZIS nanosheets while also improving the photocatalytic activity.

The loading of co-catalysts and the building of heterojunctions are serviceable solutions for solving the charge separation challenge. By coupling suitable co-catalysts with ZIS nanosheets, electrons and holes move to distinct surface sites on the catalysts, enabling an excellent separation of both oxidizing and reducing sites. Meanwhile, a high conductivity co-catalyst may efficiently avoid the accumulation of photogenerated carriers, reduces the hydrogen production overpotential, and integrates the advantages of each component into the complex, as well as performs special functions that a single photocatalyst cannot.[24] In recent years, hierarchical core–shell heterostructures with ZIS nanosheets as the shell have been widely studied, with tight interfacial contact, shortened charge transfer distances, and huge specific surface areas exposing abundant active sites, all of which are conducive to photocatalytic efficiency enhancement. Moreover, the self-assembly and aggregation phenomena of 2D ZIS nanosheets can be mitigated to a degree. For example, Zhou *et al.* have designed the core–shell type $Cu_{2-x}S@ZnIn_2S_4$ heterojunction, in which the empty core–shell structure provides an increased specific surface area with numerous reaction sites, the photocatalytic response range is wider, and the photothermal impact is prominent, which promotes the photocatalytic reactions.[25] Lou *et al.* have built a hierarchical $Co_9S_8@ZnIn_2S_4$ heterogeneous cage as an effective visible light hydrogen evolution photocatalyst. This unique structure effectively promotes photogenic charge separation and migration, offers a huge specific surface area, leads to a wealth of active sites for photocatalytic reactions, and displays superior photocatalytic water decomposition capability and durability.[26]

In light of their strong electronic conductivity, superior chemical stability, and comparatively low hydrogen production overpotential, transition metal phosphides have aroused the interest of scientists as co-catalysts.[24] Cobalt phosphide (CoP), a particular kind of transition metal phosphide, has attracted plenty of interest with respect to its abundant raw materials and straightforward fabrication procedure. However, the majority of these investigations used CoP as an isolated active center anchored onto the outer layer of the catalyst; this approach falls short of the requirement for high spatial separation in photocatalytic systems and lessens the efficiency of interfacial electron transfer in the reaction.[27–30] We plausibly believe that the architecture of heterojunctions affects photocatalytic reactions significantly, and co-catalysts with significant specific surface areas are desirable for fast electron transfer in the reaction. Thus, we recommend using CoP as a precursor with lamellar ZIS to boost photocatalytic H_2 generation activity.

Herein, we created a core–shell hierarchical structure of the CoP@ZIS heterojunction photocatalyst through *in situ* growth. As expected, the tight interfacial contact between CoP and ZIS facilitates photogenerated electron migration from ZIS to the CoP surface, effectively shortening the transfer distance and optimizing electron–hole pair separation and migration efficiency. Notably, the optimized 5-CoP@ZIS sample exhibits a remarkable hydrogen yield of 14.98 mmol g^{-1} h^{-1} under full solar spectrum treatment, which is 6.3 times greater than pure ZIS. Moreover, after 4 times of cycling, 5-CoP@ZIS maintained a high hydrogen production rate, demonstrating good stability. This work presents an appealing idea for fabricating extremely efficient ZIS-based photocatalysts for H_2 evolution *via* water decomposition.

2. Results and discussion

The synthetic route of CoP@ZIS spiny nanoflowers is schematically represented in Fig. 1. To begin with, a simple hydrothermal technique was used to create the precursor of $Co(CO_3)_{0.5}(OH)_{0.11}H_2O$ spiny nanoflowers. The $Co(CO_3)_{0.5}(OH)_{0.11}H_2O$ precursor was thermally oxidized to porous Co_3O_4, which was subsequently phosphated to create porous CoP spinous nanoflowers. Finally, the CoP@ZIS composite was constructed through *in situ* formation of ultra-thin ZIS nanosheets on the outer layer of CoP employing a low temperature solvent heat treatment, which used $ZnCl_2$, $InCl_3{\cdot}4H_2O$ and thioacetamide (TAA) as raw materials.

Fig. S1a† shows the scanning electron microscopy (SEM) picture of the $Co(CO_3)_{0.5}(OH)_{0.11}H_2O$ precursor. Obviously, the $Co(CO_3)_{0.5}(OH)_{0.11}H_2O$ precursor is assembled from smooth nanothorns into nanoflowers with a majority size ranging from 8–14 μm, while adjacent nanothorns possess adequate spaces, which is conducive to coating of the target product ZIS.[21,31] After thermal oxidation, the obtained Co_3O_4 retains the basic shape of the original $Co(CO_3)_{0.5}(OH)_{0.11}H_2O$ substrate with some rough surface (Fig. 2a–c). The (311) crystal plane of Co_3O_4 has a lattice spacing of 0.243 nm, as seen in Fig. 2d. After further phosphating, the surface of CoP becomes rougher (Fig. 2e, f and S3a†). Obviously, the presence of numerous cavities in CoP nanothorns (Fig. 2g, S3b and c†) is undoubtedly advantageous for the quick separation and transmission of photogenerated electron–hole pairs, and the existence of cavities may be attributed to the water vapor adsorbed by the CoP and the carbon source escaping in the form of gas during the high-temperature calcination process. A high-resolution transmission electron microscopy (HRTEM) picture (Fig. 2h) of

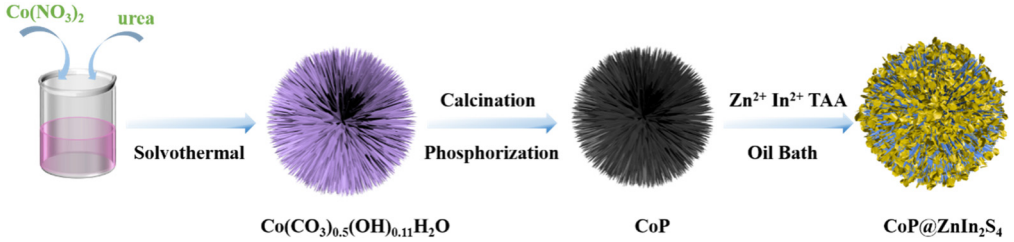

Fig. 1 Schematic diagram for the synthesis of core–shell CoP@ZIS heterostructure.

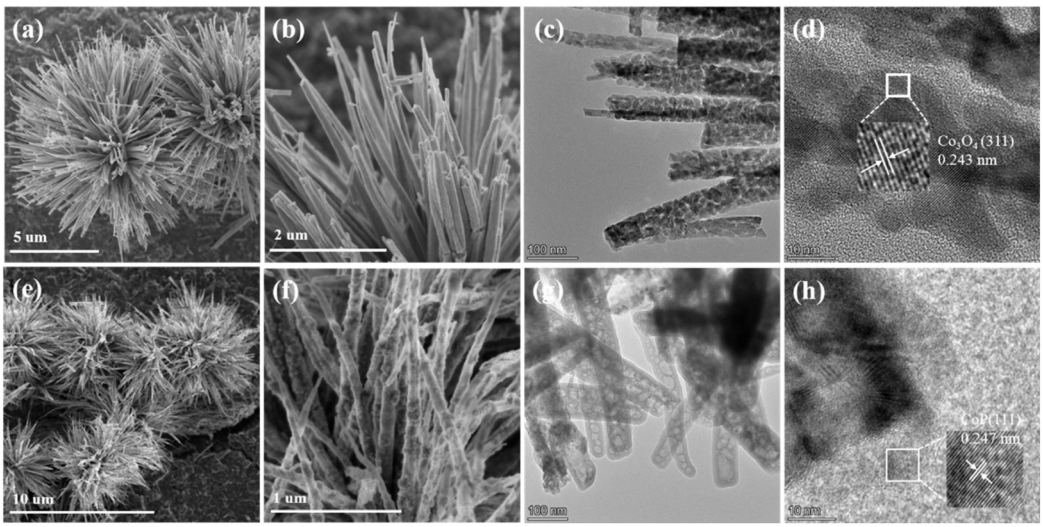

Fig. 2 SEM images of (a and b) Co_3O_4 and (e and f) CoP. TEM images of (c) Co_3O_4 and (g) CoP. HRTEM images of (d) Co_3O_4 and (h) CoP.

CoP reveals a distinct lattice spacing of 0.247 nm, belonging to the CoP (111) plane. According to the EDX elemental analysis (Fig. S3d–f†), Co and P are evenly distributed in CoP spiny flower spheres. When ZIS is coupled with CoP, it is obvious that each CoP nanothorn is evenly wrapped in ZIS nanosheets and exhibits a close contact interface (Fig. 3a and b), which is further revealed by TEM results (Fig. 3c and d). The synthesized ZIS possesses intersecting ultrathin nanosheets which are distributed uniformly on the CoP surface to construct a core–shell framework, effectively preventing the aggregation of individual ZIS, which offers improved multiple light reflections and thus optimizes the utilization of sunlight.[21,32] Importantly, the HRTEM image (Fig. 3e) collected at the contact of the CoP nanothorn and the ZIS nanosheet reveals the distinct crystal fringes of 5-CoP@ZIS with *d* values of 0.317 nm and 0.247 nm that may be nicely attributed to the (102) and (111) lattice planes of ZIS and CoP, respectively. These results imply a close contact between CoP and ZIS. Additionally, the corresponding elemental mapping images (Fig. 3f–k) confirm the coexistence and even distribution of Co, P, S, In and Zn elements, with Co and P elements being mainly distributed in the middle core region and S, In and Zn elements being distributed throughout the entire CoP, further confirming the successful synthesis of core–shell structure CoP@ZIS. The photocatalyst's precise structural design prohibits self-assembly and aggregation of 2D ultra-thin ZIS nanosheets, ensuring structural stability as well as rapid separation and migration of photogenerated electrons, hence boosting photocatalytic activity.[23] Instead, in the absence of CoP, ZIS formed nanosheet aggregates (Fig. S4a–d†).

We employed X-ray diffraction (XRD) to examine the structure of the crystals and composition of the phases of the as-obtained products. Fig. S1b† shows the prepared $Co(CO_3)_{0.5}(OH)_{0.11}H_2O$ (JCPDF# 48-0083). Fig. S2† reveals that Co_3O_4 (JCPDS# 42-1467) was successfully produced. The peaks located at 31.597°, 36.321°, 46.238°, 48.118° and 56.796° in Fig. 3l can be ascribed to the (011), (111), (112), (211) and (301) planes of orthorhombic CoP (JCPDS# 65-1474), correspondingly,[33] demonstrating the successful production of CoP after phosphating the Co_3O_4. Furthermore, all diffraction peaks observed for pure ZIS match well with the characteristic peaks of ZIS (JCPDS# 65-2023). Notably, all the CoP@ZIS composites mainly display ZIS characteristic diffraction peaks, whereas the peak intensity of CoP is modest, which may be owing to the low concentration of CoP and the fact that it is wrapped in ZIS nanosheets.[34] The degree of intensity for the (011) diffraction peak gradually increases as CoP concentration increases, while the strength of the ZIS diffraction peaks declines. It is also notable that the diffraction peak of (011) belonging to CoP in CoP@ZIS migrates to a higher angle. The modest change in peak locations and decline in peak intensity in the heterojunctions reveal that there is a certain interaction between CoP and

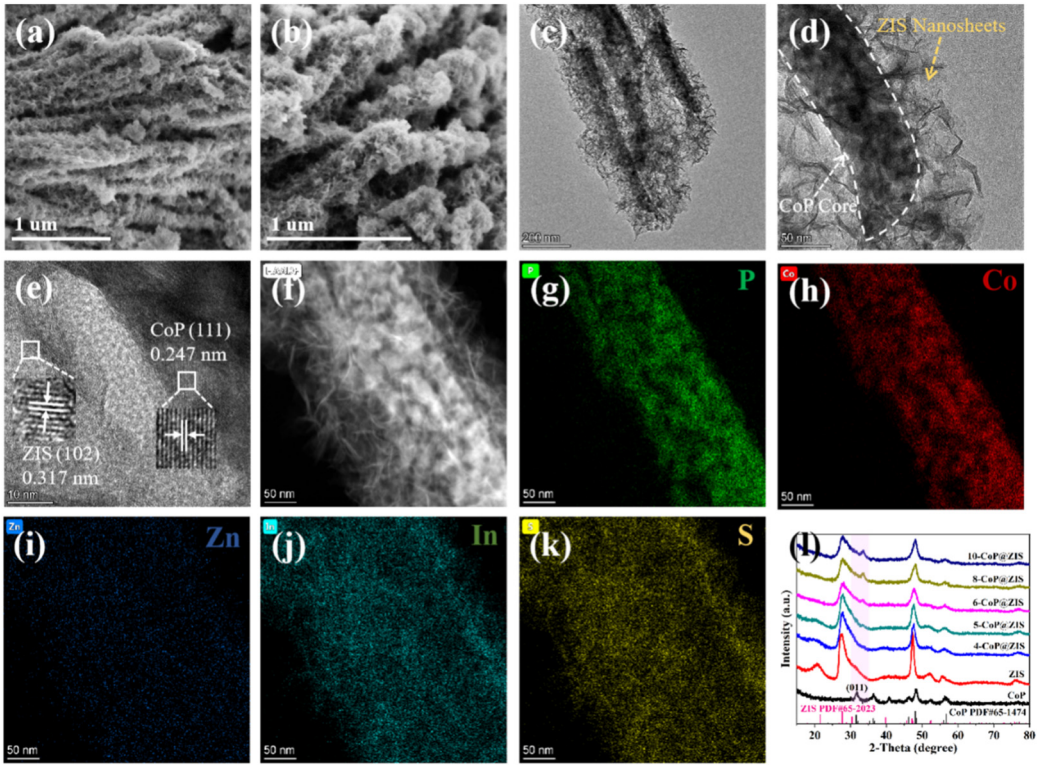

Fig. 3 (a and b) SEM, (c and d) TEM, (e) HRTEM, (f) HAADF-STEM, and (g–k) corresponding elemental mapping images of 5-CoP@ZIS. (l) XRD patterns of the different samples.

ZIS.[35] This conclusion is compatible with SEM and TEM findings, suggesting that CoP and ZIS are successfully recombined.

X-ray photoelectron spectroscopy (XPS) was employed to further explore the detailed chemical make-up of the composite surface as well as the relevant valence-state of elements. The survey XPS result of 5-CoP@ZIS clearly demonstrates the peaks of Co 2p, P 2p, S 2p, In 3d and Zn 2p (Fig. S5†). This is parallel to the finding of the elemental mapping discussed before. In the high-resolution XPS result of Zn 2p (Fig. 4a), the peaks for Zn $2p_{3/2}$ and Zn $2p_{1/2}$ in ZIS are located at 1022.17 eV and 1045.17 eV, respectively,[36] whereas those for the 5-CoP@ZIS sample are shifted to 1022.44 eV and 1045.45 eV, correspondingly. In the In 3d XPS spectra of Fig. 4b, the In $3d_{5/2}$ and In $3d_{3/2}$ peaks for ZIS are centered at 445.29 eV and 452.82 eV, respectively.[37] Similarly, the peaks centered at 445.42 eV and 452.95 eV in the In 3d XPS spectra of 5-CoP@ZIS are attributed to In $3d_{5/2}$ and In $3d_{3/2}$, correspondingly. The S 2P XPS result for pure ZIS in Fig. 4c includes two peaks at 161.88 eV and 163.08 eV, which can be ascribed to S $2p_{3/2}$ and S $2p_{1/2}$, correspondingly,[38] whereas those for the 5-CoP@ZIS sample are shifted to 161.97 eV and 163.15 eV, correspondingly. It is noteworthy that, when CoP is coupled with ZIS, the peak strength of Co2p and P 2p in 5-CoP@ZIS is low due to the instrument's detection accuracy, as well as the fact that CoP is located in the core of 5-CoP@ZIS and the depth of ZIS is massive, but the main $Co2p_{3/2}$ and $Co2p_{1/2}$ species remain readily identified. The CoP sample's Co 2p XPS spectra can be analyzed into six peaks (Fig. S6†). The values observed at 778.83 eV and 793.74 eV commonly belong to Co $2p_{3/2}$ and Co $2p_{1/2}$ for CoP, correspondingly, and those at 782.19 eV and 797.98 eV corresponded to Co $2p_{3/2}$ and Co $2p_{1/2}$ for oxidized Co species induced by the inevitable surface oxidation of CoP. Besides, two satellite peaks at 785.31 eV and 802.65 eV are triggered by high-spin Co^{2+} ion oscillations.[39] For the 5-CoP@ZIS composite, the Co 2p peaks are shifted toward the low binding energy. In Fig. 4d, the P 2p XPS result of bare CoP shows three separated peaks, with the peak at 134.34 eV being linked with oxidized P species, and the two peaks at 129.65 eV and 130.75 eV belonging to P $2p_{3/2}$ and P $2p_{1/2}$, respectively, relating to the phosphorus anion in CoP.[40] The P 2p peaks for the 5-CoP@ZIS hybrid, like the Co element, exhibit a negative change as compared to CoP. As previously described, the Zn 2p, In 3d and S 2p peaks in 5-CoP@ZIS all move slightly towards higher binding energy compared with the corresponding peaks of the original CoP and ZIS, while the peaks of Co 2p and P 2p move in the opposite way, indicating that when CoP and ZIS are coupled, the inner chemical environment of these parts changes and charges migrate in their contact section.[41] In general, increased binding energy matches decreased electron density.[42] As a result, when CoP and ZIS are coupled, ZIS serves as an electron donor and CoP serves as an electron acceptor, and electrons move from ZIS to CoP, accelerating charge carrier separation and migration, thus increasing the

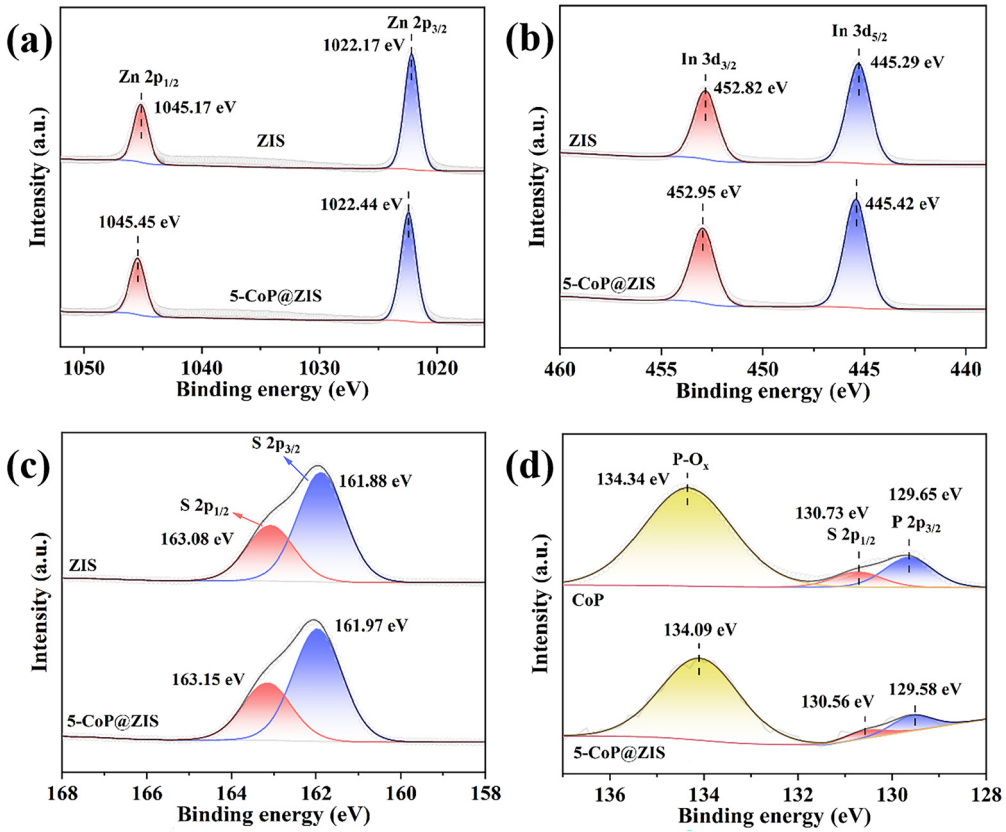

Fig. 4 High-resolution XPS spectra of (a) Zn 2p, (b) In 3d, (c) S 2p and (d) P 2p of samples.

efficiency of 5-CoP@ZIS photocatalytic decomposition of water. All of the aforementioned peak changes can be explained by the creation of the p–n heterojunction between CoP and ZIS components.

To measure the photocatalytic H_2 production capacity of the synthesized products, photocatalytic water decomposition for H_2 evolution was performed using triethanolamine (TEOA, 10 vol%) as a sacrificial agent. The time-dependent graph of the hydrogen production rate for various photocatalysts is depicted in Fig. 5a. The rate of H_2 generation increases progressively as the time of light irradiation increases. The average production rate of H_2 is shown in Fig. 5b. Due to the self-assembled 2D ZIS nanosheet structure and slow carrier migration, the average H_2 formation rate of bulk ZIS is quite low (only 2.36 mmol g^{-1} h^{-1}). And CoP produces minimal H_2 gas, indicating that it merely functions as a cocatalyst. On the contrary, CoP@ZIS possesses a substantially higher photocatalytic H_2 creation capability than either CoP or ZIS alone. Besides, the H_2 production rate increases with the content of CoP in CoP@ZIS, then decreases. This may be due to excess CoP serving as a site for charge carriers to recombine,[21] reducing the photocatalytic capacity. Therefore, the amount of CoP in the heterostructure has a significant impact on photocatalytic performance, and only a moderate amount CoP can demonstrate optimum photocatalytic hydrogen evolution performance. When the CoP content increases to 5 mg, the H_2 generation rate at 5-CoP@ZIS reaches the maximum (14.98 mmol g^{-1} h^{-1}), which is nearly 6.3-fold higher compared to the original ZIS. The synthesized CoP@ZIS heterojunctions combine numerous features that are favorable for photocatalytic hydrogen evolution reactions. First, the ZIS nanosheet shell is tightly bound to CoP and is evenly distributed on the CoP surface by ultra-thin nanosheets, which can prevent 2D ZIS nanosheet self-assembly and aggregation, enlarge the sample's active surface area, and supply greater active sites for the creation of hydrogen.[43] Second, the CoP@ZIS complex's light absorption capacity will be greatly boosted. Third, the CoP@ZIS heterojunctions will considerably increase charge transfer and migration, so that more electrons take part in the hydrogen evolution reaction, hence increasing photocatalytic activity.

Meanwhile, several kinds of controlled investigations were performed to investigate the impact of various sacrificial reagents on the performance of the 5-CoP@ZIS catalyst. The rates of generation of hydrogen are 14.98 mmol g^{-1} h^{-1}, 5.47 mmol g^{-1} h^{-1} and 1.59 mmol g^{-1} h^{-1} when the sacrificial agents are TEOA (10 vol%), lactic acid (10 vol%) and 0.25 M Na_2SO_3–0.35 M Na_2S, respectively, as displayed in Fig. 5d. Without the introduction of sacrificial agents, the yield of photocatalytic hydrogen generation is minimal. The findings indicate that the sacrificial agent is critical to the photocatalytic reaction system, and TEOA can be used as an

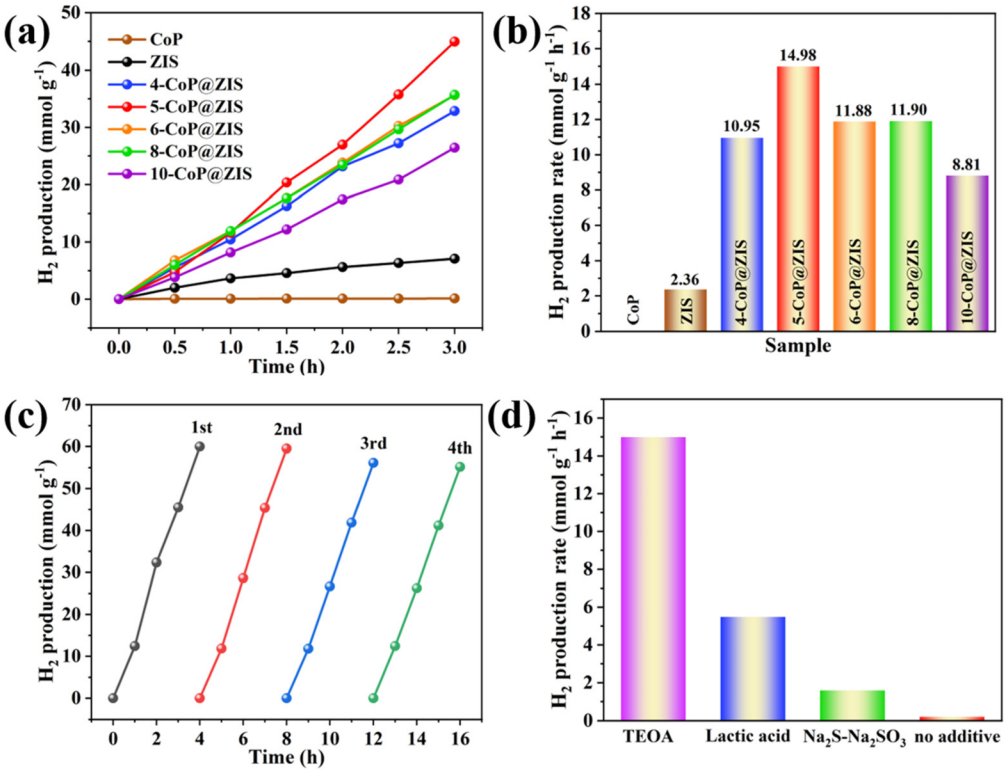

Fig. 5 Photocatalytic H_2 evolution performance: (a) time-yield plots of H_2 evolution. (b) H_2 evolution rate for different samples. (c) Cyclic tests of 5-CoP@ZIS. (d) Photocatalytic hydrogen evolution performance with different sacrificial reagents on 5-CoP@ZIS.

appropriate sacrificial agent in the present reaction system for effective hydrogen generation.

Besides the powerful photocatalytic H_2 production activity, recycling studies were done to test the stability of this 5-CoP@ZIS catalyst. As shown in Fig. 5c, the results reveal no substantial decline in hydrogen formation after four continuous rounds. Furthermore, the XRD patterns of 5-CoP@ZIS after the reaction show no discernible alteration from the original data, and the SEM images reveal that the morphology of 5-CoP@ZIS remains unchanged considerably after the activity test (Fig. S7†). The findings further confirm the satisfactory stability of the prepared 5-CoP@ZIS catalyst.

To deeply investigate the causes of the increase in photocatalytic activities, photophysical methods were utilized to evaluate the migration behaviors of charge carriers. Steady-state photoluminescence (PL) studies reveal the recombination efficiency of free excitons, and the stronger PL spectrum strength represents the faster recombination process of photogenerated electrons and holes.[18] As represented in Fig. 6a, individual ZIS shows a significant PL peak, indicating an extensive degree of charge carrier combination. The PL intensity of 5-CoP@ZIS drops dramatically compared with ZIS, manifesting a rapid separation of photogenerated electrons and holes, that's in good agreement with the photocatalytic activity data. In addition, the transient photocurrent response (Fig. 6b) and electrochemical impedance spectra (Fig. 6c) were recorded to explore the photo-induced electron/hole separation and transfer efficiency. Fig. 6b displays that 5-CoP@ZIS possesses an increased photocurrent density compared with pure ZIS, demonstrating that 5-CoP@ZIS has stronger charge carrier separation and migration dynamics.[44] The Nyquist plots

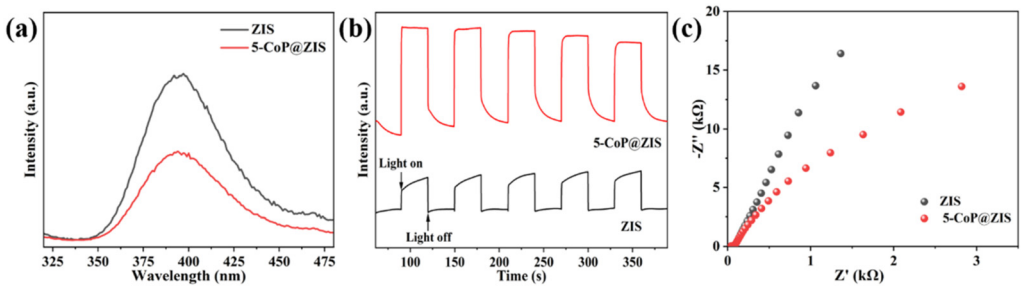

Fig. 6 (a) Steady-state PL spectra. (b) Transient photocurrent response curves. (c) EIS plots of ZIS and 5-CoP@ZIS.

(Fig. 6c) for ZIS and 5-CoP@ZIS verify that the 5-CoP@ZIS sample exhibits a smaller semi-arc, indicating that the charge transfer resistance between 5-CoP@ZIS and the electrolyte solution is lower. These findings suggest that combining ZIS with CoP greatly enhances the interfacial charge separation and transfer, thus speeding up the photocatalytic generation of the hydrogen reaction.[45]

Light capture and energy band arrangement are critical in influencing photocatalytic behaviors. The UV-vis diffuse reflectance spectrum (DRS) was obtained to analyze the optical absorption characteristics of photocatalysts (Fig. 7a). As can be observed, black CoP absorbs light across the entire spectrum, making it a powerful co-catalyst for photocatalytic decomposition of water for hydrogen formation. Meanwhile, the individual ZIS displays a clear absorption edge at around 535 nm. Because of the high light adsorption capacity of CoP,[46] all the CoP@ZIS hybrid catalysts demonstrate significantly higher light absorption, and the absorption ability steadily improves with the rise of CoP concentration in CoP@ZIS. This observation confirms that the produced heterojunction catalysts may effectively utilize light and stimulate photocatalytic processes.[47] According to the Tauc plots depicted in Fig. 7b, the band gap widths of bare CoP and ZIS are 1.46 eV and 2.62 eV, correspondingly.

Additionally, to identify the semiconductor's band arrangement, Mott–Schottky plots were also utilized. As revealed in Fig. 7c and d, the positive slope of ZIS proves it to be an n-type semiconductor,[48] whereas the negative slope of CoP is compatible with p-type semiconductor properties, indicating the presence of the p–n heterojunction.[49] Pure ZIS and CoP have flat potentials (E_{fb}) of −0.61 V (*vs.* Ag/AgCl) and 0.51 V (*vs.* Ag/AgCl), accordingly. The E_{fb} is known to be positive 0.1–0.3 V compared to the n-type semiconductor's conduction band potential (E_{CB}), and negative 0.1–0.3 V is related to the p-type semiconductor's valence band potential (E_{VB}).[49–51] Thus, the bottom of the conduction band value (CBM) of ZIS is −0.81 V (*vs.* Ag/AgCl) using $E_{CBM} = E_{fb} - 0.2$ (for n-type semiconductor), and the top of the valence band value (VBM) of CoP is 0.71 V (*vs.* Ag/AgCl) using $E_{VBM} = E_{fb} + 0.2$ (for p-type semiconductor). Then, $E_{NHE,\ CBM}$ (ZIS) = −0.21 V and $E_{NHE,\ VBM}$ (CoP) = 1.30 V, which is subsequently transformed to the standard hydrogen electrode (NHE) potential applying the following formula $E_{NHE} = E_{Ag/AgCl} + 0.0592 \times pH + 0.197$ (pH = 6.8).[52] Having known E_g, the CB of ZIS and the VB of CoP, E_{VBM} (ZIS) = 2.41 V and E_{CBM} (CoP) = −0.04 V are obtained.

In light of the findings presented above, the photocatalytic hydrogen production process of the CoP@ZIS catalyst was preliminarily investigated, and the possible charge carrier movement pathways were proposed,[35] as shown in Fig. 8. Firstly, CoP@ZIS absorbs energy from solar irradiation, and when the absorbed energy is more than that of CoP@ZIS, electrons in ZIS are driven to the conduction band (CB), leaving holes in the valence band (VB).[53,54] Owing to the good energy level arrangement and high-quality interface in the CoP@ZIS photocatalyst, the electrons on the CB in ZIS

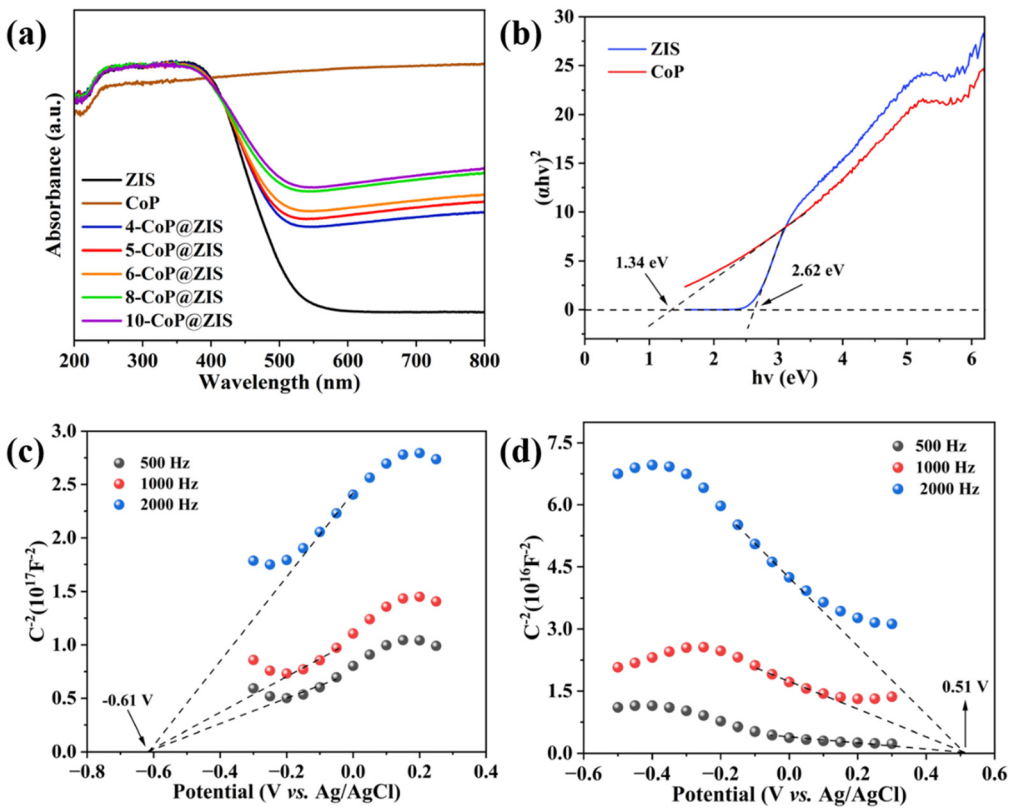

Fig. 7 (a) UV-vis diffuse reflectance spectra, and (b) the corresponding Tauc plots of different samples. Mott–Schottky plots of (c) ZIS and (d) CoP.

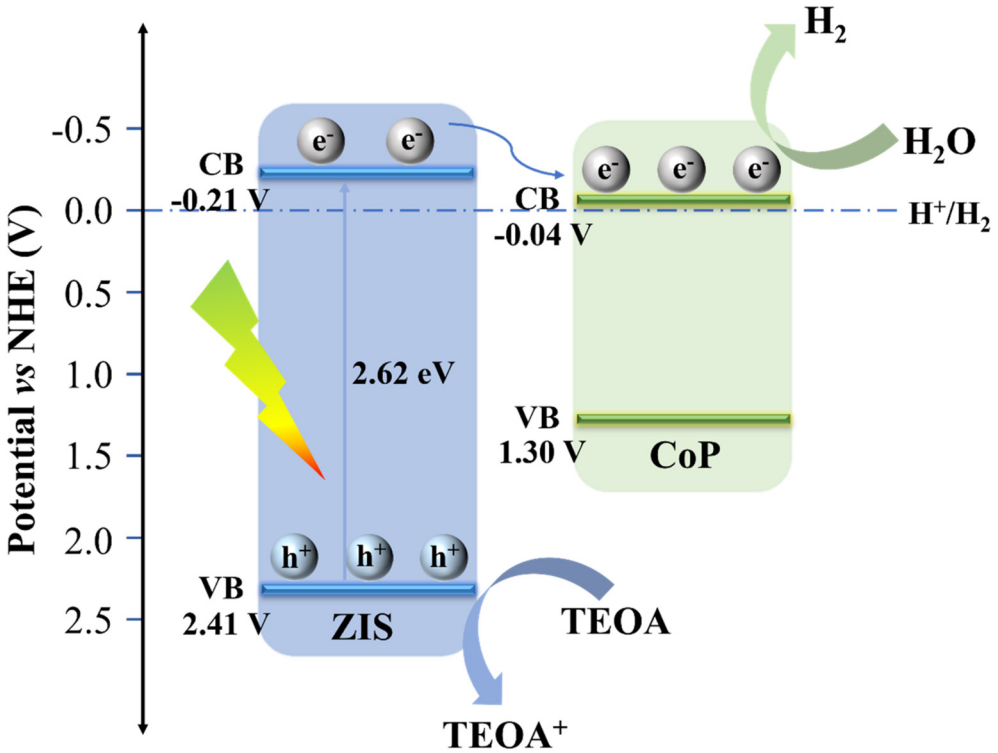

Fig. 8 Schematic diagram of the possible charge flow paths.

quickly move to the CB in CoP, the directional and efficient electron migration from the shell of ZIS to the nucleus of CoP takes place in order to reduce the protons and release the hydrogen, and the holes left in the VB in ZIS are trapped by the sacrificial agent, leading to a long-distance separation of oxidative and reductive sites and increase of photocatalytic performance.[55] Because of its metal-like nature and narrow band gap, CoP contributes little to the formation of reducing electrons under photoexcitation, and its beneficial function is to increase electron conduction on the surface so as to finish the protonation reaction.[42] Furthermore, the CoP@ZIS core–shell structure possesses a higher diffusion surface area, which ensures that the photogenerated electrons may transport efficiently at the interface and considerably improves the separation efficiency of electron–hole pairs, thus enhancing PHE capability.

3. Conclusions

In light of the limited charge separation of photocatalysts, efficient H_2 production remains a long-term difficulty. This difficulty is well addressed in this work by the *in situ* fabrication of ZIS nanosheets on spiny CoP nanoflowers using a spatial decoupling technique. The created core–shell CoP@ZIS heterostructure effectively limits ZIS nanosheet aggregation, exposing more active sites spatially separating oxidation and reduction sites. Under complete solar spectrum irradiation, the optimized 5-CoP@ZIS sample acquires an excellent hydrogen yield of 14.98 mmol g^{-1} h^{-1}, which is nearly 6.3-fold greater compared to the single ZIS. This study illustrates the feasibility of building CoP@ZIS heterojunction photocatalysts to facilitate charge separation for fast H_2 production so as to solve the increasing energy scarcity and environmental concerns.

Conflicts of interest

There are no conflicts to declare.

Acknowledgements

This work was supported by the National Natural Science Foundation of China (No. 22272207, 22106087), the Fundamental Research Funds for the Central Universities, South-Central MinZu University (No. CZZ23008), and the Joint Funds of the Zhejiang Provincial Natural Science Foundation of China (No. LZY22B070001).

References

1 F. Leng, H. Liu, M. Ding, Q.-P. Lin and H.-L. Jiang, Boosting Photocatalytic Hydrogen Production of Porphyrinic MOFs: The Metal Location in Metalloporphyrin Matters, *ACS Catal.*, 2018, **8**, 4583–4590, DOI: **10.1021/acscatal.8b00764**.

2 L. Lin, W. Ren, C. Wang, A. M. Asiri, J. Zhang and X. Wang, Crystalline Carbon Nitride Semiconductors Prepared at Different Temperatures for Photocatalytic Hydrogen Production, *Appl. Catal., B*, 2018, **231**, 234–241, DOI: **10.1016/j.apcatb.2018.03.009**.

3 C. Feng, Z. Chen, J. Hou, J. Li, X. Li, L. Xu, M. Sun and R. Zeng, Effectively Enhanced Photocatalytic Hydrogen Production Performance of One-Pot Synthesized MoS_2 Clusters/CdS Nanorod Heterojunction Material under Visible Light, *Chem. Eng. J.*, 2018, **345**, 404–413, DOI: **10.1016/j.cej.2018.03.155**.

4 Y. Zhu, J. Yin, E. Abou-Hamad, X. Liu, W. Chen, T. Yao, O. F. Mohammed and H. N. Alshareef, Highly Stable Phosphonate-Based MOFs with Engineered Bandgaps for Efficient Photocatalytic Hydrogen Production, *Adv. Mater.*, 2020, **32**, 1906368, DOI: **10.1002/adma.201906368**.

5 P. Zhou, H. Chen, Y. Chao, Q. Zhang, W. Zhang, F. Lv, L. Gu, Q. Zhao, N. Wang and J. Wang, *et al.* Single-Atom Pt-I3 Sites on All-Inorganic Cs2SnI6 Perovskite for Efficient Photocatalytic Hydrogen Production, *Nat. Commun.*, 2021, **12**, 4412, DOI: **10.1038/s41467-021-24702-8**.

6 Y. Jiang, M. Li, Y. Mi, L. Guo, W. Fang, X. Zeng, T. Zhou and Y. Liu, The Influence of Piezoelectric Effect on the Heterogeneous Photocatalytic Hydrogen Production of Strontium Titanate Nanoparticles, *Nano Energy*, 2021, **85**, 105949, DOI: **10.1016/j.nanoen.2021.105949**.

7 D. Kim and K. Yong, Boron Doping Induced Charge Transfer Switching of a C_3N_4/ZnO Photocatalyst from Z-Scheme to Type II to Enhance Photocatalytic Hydrogen Production, *Appl. Catal., B*, 2021, **282**, 119538, DOI: **10.1016/j.apcatb.2020.119538**.

8 Y. Chen, S. Ji, W. Sun, Y. Lei, Q. Wang, A. Li, W. Chen, G. Zhou, Z. Zhang and Y. Wang, *et al.* Engineering the Atomic Interface with Single Platinum Atoms for Enhanced Photocatalytic Hydrogen Production, *Angew. Chem., Int. Ed.*, 2020, **59**, 1295–1301, DOI: **10.1002/anie.201912439**.

9 J. Yao, J. Chen, K. Shen and Y. Li, Phase-Controllable Synthesis of MOF-Templated Maghemite–Carbonaceous Composites for Efficient Photocatalytic Hydrogen Production, *J. Mater. Chem. A*, 2018, **6**, 3571–3582, DOI: **10.1039/C7TA10284D**.

10 J. Zhou, J. Zhao and R. Liu, Defect Engineering of Zeolite Imidazole Framework Derived ZnS Nanosheets towards Enhanced Visible Light Driven Photocatalytic Hydrogen Production, *Appl. Catal., B*, 2020, **278**, 119265, DOI: **10.1016/j.apcatb.2020.119265**.

11 X. Xue, W. Dong, Q. Luan, H. Gao and G. Wang, Novel Interfacial Lateral Electron Migration Pathway Formed by Constructing Metallized CoP_2/CdS Interface for Excellent Photocatalytic Hydrogen Production, *Appl. Catal., B*, 2023, **334**, 122860, DOI: **10.1016/j.apcatb.2023.122860**.

12 J. Hu, Z. Xin, N. Liu and L. Gao, Construction of $CdIn_2S_4$/WO_3 Z-type Heterojunction for the Photocatalytic Degradation of Tetracycline, *Xuzhou Gongcheng Xueyuan Xuebao, Ziran Kexueban*, 2023, **3**, 68–77, DOI: **10.15873/j.cnki.jxit.000521**.

13 M. Ren, X. Zhang, Y. Liu, G. Yang, L. Qin, J. Meng, Y. Guo and Y. Yang, Interlayer Palladium-Single-Atom-Coordinated Cyano-Group-Rich Graphitic Carbon Nitride for Enhanced Photocatalytic Hydrogen Production Performance, *ACS Catal.*, 2022, **12**, 5077–5093, DOI: **10.1021/acscatal.2c00427**.

14 L. Zhu, Q. Yue, D. Jiang, H. Chen, R. M. Irfan and P. Du, Metal-Free Graphene Quantum Dots Photosensitizer Coupled with Nickel Phosphide Cocatalyst for Enhanced Photocatalytic Hydrogen Production in Water under Visible Light, *Chin. J. Catal.*, 2018, **39**, 1753–1761, DOI: **10.1016/S1872-2067(18)63135-3**.

15 Y. Shi, L. Li, Z. Xu, F. Guo and W. Shi, Construction of Full Solar-Spectrum Available S-Scheme Heterojunction for Boosted Photothermal-Assisted Photocatalytic H_2 Production, *Chem. Eng. J.*, 2023, **459**, 141549, DOI: **10.1016/j.cej.2023.141549**.

16 L. Zhu, H. Li, Z. Liu, P. Xia, Y. Xie and D. Xiong, Synthesis of the 0D/3D CuO/ZnO Heterojunction with Enhanced Photocatalytic Activity, *J. Phys. Chem. C*, 2018, **122**, 9531–9539, DOI: **10.1021/acs.jpcc.8b01933**.

17 W. Huang, Z. Li, C. Wu, H. Zhang, J. Sun and Q. Li, Delaminating Ti_3C_2 MXene by Blossom of $ZnIn_2S_4$ Microflowers for Noble-Metal-Free Photocatalytic Hydrogen Production, *J. Mater. Sci. Technol.*, 2022, **120**, 89–98, DOI: **10.1016/j.jmst.2021.12.028**.

18 Z. Li, F. Huang, Y. Xu, A. Yan, H. Dong, X. Xiong and X. Zhao, Electron-Extracting System with Enhanced Photocatalytic Hydrogen Production Performance: Synergistic Utilization of Z-Scheme and Ohmic Heterojunctions, *Chem. Eng. J.*, 2022, **429**, 132476, DOI: **10.1016/j.cej.2021.132476**.

19 J. Qiu, M. Li, L. Yang and J. Yao, Facile Construction of Three-Dimensional Netted $ZnIn_2S_4$ by Cellulose Nanofibrils for Efficiently Photocatalytic Reduction of Cr (VI), *Chem. Eng. J.*, 2019, **375**, 121990, DOI: **10.1016/j.cej.2019.121990**.

20 C. Du, B. Yan and G. Yang, Self-Integrated Effects of 2D $ZnIn_2S_4$ and Amorphous Mo_2C Nanoparticles Composite for Promoting Solar Hydrogen Generation, *Nano Energy*, 2020, **76**, 105031, DOI: **10.1016/j.nanoen.2020.105031**.

21 X. Feng, H. Shang, J. Zhou, X. Ma, X. Gao, D. Wang, B. Zhang and Y. Zhao, Heterostructured Core–Shell $CoS_{1.097}$@$ZnIn_2S_4$ Nanosheets for Enhanced Photocatalytic Hydrogen Evolution under Visible Light, *Chem. Eng. J.*, 2023, **457**, 141192, DOI: **10.1016/j.cej.2022.141192**.

22 C. Men, L. Chen, H. Ji, Z. Qin and T. Su, Synergistic Effect of Internal Electric Field and Ligand-to-Metal Charge Transfer in Z-Scheme CuPc/$ZnIn_2S_4$ for Boosting Photocatalytic Hydrogen Evolution, *Chem. Eng. J.*, 2023, 145173, DOI: **10.1016/j.cej.2023.145173**.

23 J. Mao, J. Iocozzia, J. Huang, K. Meng, Y. Lai and Z. Lin, Graphene Aerogels for Efficient Energy Storage and Conversion, *Energy Environ. Sci.*, 2018, **11**, 772–799, DOI: **10.1039/C7EE03031B**.

24 J. Tao, M. Wang, X. Zhang, L. Lu, H. Tang, Q. Liu, S. Lei, G. Qiao and G. Liu, A Novel CoP@AAH Cocatalyst Leads to Excellent Stability and Enhanced Photocatalytic H_2 Evolution of CdS by Structurally Separating the Photogenerated Carriers, *Appl. Catal., B*, 2023, **320**, 122004, DOI: **10.1016/j.apcatb.2022.122004**.

25 Y. Wang, M. Liu, C. Wu, J. Gao, M. Li, Z. Xing, Z. Li and W. Zhou, Hollow Nanoboxes $Cu_{2-x}S$@$ZnIn_2S_4$ Core-Shell

S-Scheme Heterojunction with Broad-Spectrum Response and Enhanced Photothermal-Photocatalytic Performance, *Small*, 2022, **18**, 2202544, DOI: **10.1002/smll.202202544**.

26 S. Wang, B. Y. Guan, X. Wang and X. W. D. Lou, Formation of Hierarchical Co_9S_8 @$ZnIn_2S_4$ Heterostructured Cages as an Efficient Photocatalyst for Hydrogen Evolution, *J. Am. Chem. Soc.*, 2018, **140**, 15145–15148, DOI: **10.1021/jacs.8b07721**.

27 K. Qi, W. Lv, I. Khan and S. Liu, Photocatalytic H_2 Generation via CoP Quantum-Dot-Modified g-C_3N_4 Synthesized by Electroless Plating, *Chin. J. Catal.*, 2020, **41**, 114–121, DOI: **10.1016/S1872-2067(19)63459-5**.

28 S. Cao, Y. Chen, H. Wang, J. Chen, X. Shi, H. Li, P. Cheng, X. Liu, M. Liu and L. Piao, Ultrasmall CoP Nanoparticles as Efficient Cocatalysts for Photocatalytic Formic Acid Dehydrogenation, *Joule*, 2018, **2**, 549–557, DOI: **10.1016/j.joule.2018.01.007**.

29 F. Guo, X. Huang, Z. Chen, H. Sun and L. Chen, Prominent Co-Catalytic Effect of CoP Nanoparticles Anchored on High-Crystalline g-C_3N_4 Nanosheets for Enhanced Visible-Light Photocatalytic Degradation of Tetracycline in Wastewater, *Chem. Eng. J.*, 2020, **395**, 125118, DOI: **10.1016/j.cej.2020.125118**.

30 B. Luo, R. Song, J. Geng, X. Liu, D. Jing, M. Wang and C. Cheng, Towards the Prominent Cocatalytic Effect of Ultra-Small CoP Particles Anchored on g-C_3N_4 Nanosheets for Visible Light Driven Photocatalytic H_2 Production, *Appl. Catal., B*, 2019, **256**, 117819, DOI: **10.1016/j.apcatb.2019.117819**.

31 M. Wang, G. Zhang, Z. Guan, J. Yang and Q. Li, Spatially Separating Redox Centers and Photothermal Effect Synergistically Boosting the Photocatalytic Hydrogen Evolution of $ZnIn_2S_4$ Nanosheets, *Small*, 2021, **17**, 2006952, DOI: **10.1002/smll.202006952**.

32 X. Zhou, L. Yin, K. Dai, X. Gao, Y. Feng, Y. Zhao and B. Zhang, Preparation of Ni_2P on Twinned $Zn_{0.5}Cd_{0.5}S$ Nanocrystals for High-Efficient Photocatalytic Hydrogen Production, *J. Chem. Sci.*, 2020, **132**, 26, DOI: **10.1007/s12039-019-1727-1**.

33 L. Zhang, G. Wang, X. Hao, Z. Jin and Y. Wang, MOFs-Derived Cu_3P@CoP p-n Heterojunction for Enhanced Photocatalytic Hydrogen Evolution, *Chem. Eng. J.*, 2020, **395**, 125113, DOI: **10.1016/j.cej.2020.125113**.

34 S. Prabu and K.-Y. Chiang, Yolk-Shell Silica Dioxide Spheres @ Metal-Organic Framework Immobilized Ni/Mo Nanoparticles as an Effective Catalyst for Formic Acid Dehydrogenation at Low Temperature, *J. Colloid Interface Sci.*, 2021, **604**, 584–595, DOI: **10.1016/j.jcis.2021.06.160**.

35 M. Cao, F. Yang, Q. Zhang, J. Zhang, L. Zhang, L. Li, X. Wang and W.-L. Dai, Facile Construction of Highly Efficient MOF-Based Pd@UiO-66-NH_2@$ZnIn_2S_4$ Flower-like Nanocomposites for Visible-Light-Driven Photocatalytic Hydrogen Production, *J. Mater. Sci. Technol.*, 2021, **76**, 189–199, DOI: **10.1016/j.jmst.2020.11.028**.

36 J. Huang, Q. Tian, H. Feng, C. Xue, J. Li and Q. Xu, Boosting Light Harvesting and Charge Separation in 3D Porous WS_2@C@$ZnIn_2S_4$ Skeleton Heterojunction for Efficient Solar Fuels Production, *Chem. Eng. J.*, 2022, **447**, 137568, DOI: **10.1016/j.cej.2022.137568**.

37 Q. Luan, X. Xue, R. Li, L. Gu, W. Dong, D. Zhou, X. Wang, B. Li, G. Wang and C. Hou, Boosting Photocatalytic Hydrogen Evolution: Orbital Redistribution of Ultrathin $ZnIn_2S_4$ Nanosheets via Atomic Defects, *Appl. Catal., B*, 2022, **305**, 121007, DOI: **10.1016/j.apcatb.2021.121007**.

38 J. Pan, G. Zhang, Z. Guan, Q. Zhao, G. Li, J. Yang, Q. Li and Z. Zou, Anchoring Ni Single Atoms on Sulfur-Vacancy-Enriched $ZnIn_2S_4$ Nanosheets for Boosting Photocatalytic Hydrogen Evolution, *J. Energy Chem.*, 2021, **58**, 408–414, DOI: **10.1016/j.jechem.2020.10.030**.

39 Q. Zhou, R. Sun, Y. Ren, R. Tian, J. Yang, H. Pang, K. Huang, X. Tian, L. Xu and Y. Tang, Reactive Template-derived Interfacial Engineering of CoP/CoO Heterostructured Porous Nanotubes towards Superior Electrocatalytic Hydrogen Evolution, *Carbon Energy*, 2023, **5**, e273, DOI: **10.1002/cey2.273**.

40 H. Cai, L. Xiong, B. Wang, D. Zhu, H. Hao, X. Yu, C. Li and S. Yang, N-Doped CNT as Electron Transport Promoter by Bridging CoP and Carbon Cloth toward Enhanced Alkaline Hydrogen Evolution, *Chem. Eng. J.*, 2022, **430**, 132824, DOI: **10.1016/j.cej.2021.132824**.

41 W. Li, Y. Chen, W. Han, S. Liang, Y. Jiao and G. Tian, ZIF-8 Derived Hierarchical ZnO@$ZnFe_2O_4$ Hollow Polyhedrons Anchored with CdS for Efficient Photocatalytic CO_2 Reduction, *Sep. Purif. Technol.*, 2023, **309**, 122970, DOI: **10.1016/j.seppur.2022.122970**.

42 Q. Zhang, X. Wang, J. Zhang, L. Li, H. Gu and W.-L. Dai, Hierarchical Fabrication of Hollow Co_2P Nanocages Coated with $ZnIn_2S_4$ Thin Layer: Highly Efficient Noble-Metal-Free Photocatalyst for Hydrogen Evolution, *J. Colloid Interface Sci.*, 2021, **590**, 632–640, DOI: **10.1016/j.jcis.2021.01.083**.

43 D. Zhou, X. Xue, X. Wang, Q. Luan, A. Li, L. Zhang, B. Li, W. Dong, G. Wang and C. Hou, Ni, In Co-Doped $ZnIn_2S_4$ for Efficient Hydrogen Evolution: Modulating Charge Flow and Balancing H Adsorption/Desorption, *Appl. Catal., B*, 2022, **310**, 121337, DOI: **10.1016/j.apcatb.2022.121337**.

44 X. Peng, L. Ye, Y. Ding, L. Yi, C. Zhang and Z. Wen, Nanohybrid Photocatalysts with $ZnIn_2S_4$ Nanosheets Encapsulated UiO-66 Octahedral Nanoparticles for Visible-Light-Driven Hydrogen Generation, *Appl. Catal., B*, 2020, **260**, 118152, DOI: **10.1016/j.apcatb.2019.118152**.

45 J. Zhang, H. Gu, X. Wang, H. Zhang, S. Chang, Q. Li and W.-L. Dai, Robust S-Scheme Hierarchical Au-$ZnIn_2S_4$/$NaTaO_3$: Facile Synthesis, Superior Photocatalytic H_2 Production and Its Charge Transfer Mechanism, *J. Colloid Interface Sci.*, 2022, **625**, 785–799, DOI: **10.1016/j.jcis.2022.06.074**.

46 Y. Geng, X. Zou, Y. Lu and L. Wang, Fabrication of the SnS_2/$ZnIn_2S_4$ Heterojunction for Highly Efficient Visible Light Photocatalytic H_2 Evolution, *Int. J. Hydrogen Energy*, 2022, **47**, 11520–11527, DOI: **10.1016/j.ijhydene.2022.01.176**.

47 X. Zhang, F. Tian, M. Gao, W. Yang and Y. Yu, L-Cysteine Capped Mo_2C/$Zn_{0.67}Cd_{0.33}S$ Heterojunction with Intimate Covalent Bonds Enables Efficient and Stable H_2-Releasing

Photocatalysis, *Chem. Eng. J.*, 2022, **428**, 132628, DOI: **10.1016/j.cej.2021.132628**.

48 H. Park, S. Kim, T. Kim, Y. Kim, S. W. Joo and M. Kang, CoS@TiO_2 S-Scheme Heterojunction Photocatalyst for Hydrogen Production from Photoinduced Water Splitting, *J. Cleaner Prod.*, 2021, **319**, 128819, DOI: **10.1016/j.jclepro.2021.128819**.

49 C. Zhao, A. Zhou, Y. Dou, J. Zhou, J. Bai and J.-R. Li, Dual MOFs Template-Directed Fabrication of Hollow-Structured Heterojunction Photocatalysts for Efficient CO_2 Reduction, *Chem. Eng. J.*, 2021, **416**, 129155, DOI: **10.1016/j.cej.2021.129155**.

50 J. Zheng, T. Chen and H. Chen, Antibiotic Resistome Promotion in Drinking Water during Biological Activated Carbon Treatment: Is It Influenced by Quorum Sensing, *Sci. Total Environ.*, 2018, **612**, 1–8, DOI: **10.1016/j.scitotenv.2017.08.072**.

51 S. Zhang, S. Du, Y. Wang, Z. Han, X. Li, G. Li, Q. Hu, H. Xu, C. He and P. Fang, Synergy of Yolk-Shelled Structure and Tunable Oxygen Defect over CdS/$CdCO_3$-CoS_2: Wide Band-Gap Semiconductors Assist in Efficient Visible-Light-Driven H_2 Production and CO_2 Reduction, *Chem. Eng. J.*, 2023, **454**, 140113, DOI: **10.1016/j.cej.2022.140113**.

52 W. Zhou, J. Jia, J. Lu, L. Yang, D. Hou, G. Li and S. Chen, Recent Developments of Carbon-Based Electrocatalysts for Hydrogen Evolution Reaction, *Nano Energy*, 2016, **28**, 29–43, DOI: **10.1016/j.nanoen.2016.08.027**.

53 Md. Hoque and M. Guzman, Photocatalytic Activity: Experimental Features to Report in Heterogeneous Photocatalysis, *Materials*, 2018, **11**, 1990, DOI: **10.3390/ma11101990**.

54 X. Zheng, Y. Song, Y. Liu, Y. Yang, D. Wu, Y. Yang, S. Feng, J. Li, W. Liu and Y. Shen, *et al.* ZnIn2S4-Based Photocatalysts for Photocatalytic Hydrogen Evolution via Water Splitting, *Coord. Chem. Rev.*, 2023, **475**, 214898, DOI: **10.1016/j.ccr.2022.214898**.

55 W. Liu, Y. Wang, H. Huang, J. Wang, G. He, J. Feng, T. Yu, Z. Li and Z. Zou, Spatial Decoupling of Redox Chemistry for Efficient and Highly Selective Amine Photoconversion to Imines, *J. Am. Chem. Soc.*, 2023, **145**, 7181–7189, DOI: **10.1021/jacs.2c12182**.